Guiding Chiral Self-Propellers in a Periodic Potential

Amir Nourhani,[1,*] Vincent H. Crespi,[1,2,3] and Paul E. Lammert[1]
[1]Department of Physics, Pennsylvania State University, University Park, Pennsylvania 16802, USA
[2]Department of Materials Science and Engineering, Pennsylvania State University, University Park, Pennsylvania 16802, USA
[3]Department of Chemistry, Pennsylvania State University, University Park, Pennsylvania 16802, USA
(Received 3 November 2014; published 8 September 2015)

Ingenious suggestions continue to be made for separation of racemic mixtures according to the inert structural chirality of the constituents. Recently discovered self-motile micro- or nanoparticles express *dynamical* chirality, i.e., that which originates in motion, not structure. Here, we predict how dynamically chiral objects, with overdamped dynamics in a soft periodic two-dimensional potential, can display not only separation into well-defined dynamical subclasses defined by motility characteristics, but also the ability to be steered to arbitrary locations in the plane by simply changing the amplitude of the external potential. Orientational and translational diffusion produce new types of drift absent in the noise-free case. As practical implementation seems feasible with acoustic or optical fields, these phenomena can be useful for laboratory microscales manipulations, possibly including reconfigurable microfluidic circuits with complex networks of unidirectional channels.

DOI: 10.1103/PhysRevLett.115.118101 PACS numbers: 47.63.mf, 05.40.-a, 82.70.Dd

Chirality—the lack of mirror symmetry—is of fundamental and practical importance across physics, biotechnology, medicine, and nanotechnology. For example, objects with differing *structural* chirality can exhibit radically differing biological activity. Hence, several techniques have been developed to efficiently sort chiral molecules [1] and micro- or nanoparticles [2–7] using external fields to drive the particles through potential landscapes where the field-plus-landscape breaks chiral symmetry. Certain *self-motile* biological or artificial objects express a *dynamic* chirality by swimming in circles [8–19], while not necessarily having a chiral shape. Here, we demonstrate that a rich suite of behaviors, going well beyond simple separation, can be elicited from these "circle swimmers" or "chiral self-propellers" by adjusting the strength and period parameters of an appropriately asymmetric periodic potential in which they move.

A chiral self-propeller in the absence of thermal noise or external potential simply returns to its original position after each circular orbit. Addition of orientational diffusion produces an effective translational diffusion [20–26] (with a subtle hidden chirality [26]) without a steady drift. Pioneering simulation efforts examined the interaction of orbiting microswimmers with regular arrays of hard obstacles, such as L-shaped barriers [27] or pinwheels [28]. These investigations reveal very interesting physics: distinct behaviors for right- and left-handed swimmers and a sensitive, fine-grained dependence on orbital radius and barrier shape. For deterministic motion, the sharp corners and edges of a periodic hard-wall potential tend to yield a very jagged landscape for different types of swimmer response as a function of orbital radius or lattice constant; weak stochastic forces wash out these thinly sliced discrete classes of behavior. The complex interaction of a hard wall with the orientation of a nonpointlike swimmer adds additional complication.

We show how a wide variety of drift behaviors are possible for a chiral swimmer in a *smooth* overdamped periodic potential. Tuning the strength of the potential *in situ*—something straightforward for soft potentials imposed by acoustic or optical fields—can steer populations of rotors to arbitrary points in a plane through a judicious sequence of drifts; it can separate swimmers based on their linear or angular speed, chirality, or stochastic response; potentially, one could construct boundaryless fluidic circuits by defining different drift directions in different regions of space. Furthermore, the dynamical chiralities of rotary swimmers can be interconverted through flipping (rotation by π) about the motive axis of the swimmer (as has been observed experimentally for, e.g., bimetallic circle swimmers [25]), thereby possibly promoting chirality to a switchable state variable. The generation of linear drift from rotary motion is a fundamental coupling of great practical and fundamental importance for powered systems across a broad range of length scales from aircraft carrier to spermatozoon—here, we present a scheme to achieve this coupling in a robust manner at the micro- and nanoscale, with a drift direction that does not align to the rotational axis.

To obtain controlled drift in two dimensions, the periodic potential in which the swimmer moves must not be invariant under inversion (= rotation by π). Note, this is *not* the same as being chiral: a swastika is chiral but inversion invariant, whereas our potential is achiral. Since spatial inversion of a two-dimensional orbit leaves its chirality unchanged, the only drift velocity allowed in

an inversion-symmetric potential is zero. (Inert structurally chiral particles can be separated in inversion-symmetric potentials, by applying an additional driving field which breaks the symmetry [4,5].) If one wishes to prevent multiple drift directions for a single chirality, the potential should also lack all rotation symmetry. But a mirror symmetry, say reflection across the x axis, helps ensure separation of the chiralities. Since the reflection reverses the handedness of the swimmer even as it preserves the potential, the drift velocities of clockwise and counterclockwise rotators will have opposite y components, but equal x components. Thus, swimmers of different chiralities part ways, yet their drifts are not completely dissimilar. Even if, in the very long run, a swimmer switches chirality from time to time due to random perturbations flipping it over, there will still be a long-term net drift in the x direction as long as either drift has a nonzero x component. Surprisingly, an even less-symmetric potential provides no such guarantee of separation by chirality. Time reversal of the swimmer's mesoscale rigid-body dynamics in a reflection-symmetric potential reverses both components of the microscopic velocity, but only one component of the drift velocity at long length and time scales—an interesting discrepancy between short and long time scale symmetries under time reversal.

In the absence of a potential, a chiral swimmer translates with velocity $\boldsymbol{v}_0 = v_0\hat{v}$ and rotates with angular velocity $s_\omega\omega$, where $\omega > 0$ and $s_\omega = \pm 1$ for clockwise $(-)$ or counterclockwise $(+)$ rotation. $\hat{v}$ is the swimmer's *intrinsic orientation*. Under overdamped dynamics, a static external potential $V(\boldsymbol{r})$ supplies an additive contribution $-\mu\boldsymbol{\nabla}V(\boldsymbol{r})$ to the velocity, where μ is the Stokes mobility of the swimmer, so that the velocity is generally no longer along the intrinsic orientation. The potential is taken as a superposition of standing waves $\mu V(\boldsymbol{r}) = C\sum_{i=1}^{3} c_i \cos(K\hat{k}_i \cdot \boldsymbol{r} + \delta_i)$, with $\sum_{i=1}^{3} c_i^2 = 1$. K is the the inverse spatial scale ("finesse"), and C the strength of the potential. More convenient are dimensionless versions, comparing the potential-induced velocity scale to the free-swimmer speed, and the free-swimmer orbit radius to the potential period:

$$\alpha = \frac{CK}{v_0}, \qquad \beta = \frac{Kv_0}{\omega}. \tag{1}$$

The shape and symmetry of the potential are determined by the unit vectors $\hat{k}_i$, the ratios of the c_i's, and the phase offsets δ_i. Using units of ω^{-1} for time and v_0/ω (free swimmer orbit radius) for length, the equations of motion, including orientational and translational diffusion, are

$$\begin{aligned} \frac{d\boldsymbol{r}}{dt} &= \hat{v}(\theta) + \boldsymbol{\xi}(t) + \alpha\sum_{i=1}^{3} c_i\hat{k}_i \sin(\beta\hat{k}\cdot\boldsymbol{r} + \delta_i) \\ \frac{d\theta}{dt} &= s_\omega + \zeta(t). \end{aligned} \tag{2}$$

Here, ζ and ξ_i are independent zero-mean white noises in translation and orientation, with dimensionless strengths $\gamma_o = D_o/\omega$ and $\gamma_t = D_t\omega/v_0^2$, D_o and D_t being conventional diffusion coefficients. For typical microfluidic swimmers, $\gamma_o \sim 10^{-2}$ and $\gamma_t \sim 10^{-3}$ to 10^{-2} [8]. Taking $\hat{k}_1 = (1,0)$, $\hat{k}_2 = (-1/2, \sqrt{3}/2)$, $\hat{k}_3 = \hat{k}_2 - \hat{k}_1$; $\delta_1 = \delta_2 = 0$, $\delta_3 = 1.3$; and $c_1 = 0.256$, $c_2 = c_3 = 0.683$ gives a potential with minima and maxima lying on interpenetrating triangular lattices, with a mirror line parallel to $\hat{x}$, but none parallel to $\hat{y}$ (thus satisfying the requirements discussed earlier). Gray scale plots appear in Fig. 1. The unequal amplitudes and phase offset break inversion and rotation symmetries while maintaining the mirror line along $\hat{x}$. Local minima of the potential are interconnected by the four saddle points channeling transitions between local minima. We present explicit results for clockwise rotation, $s_\omega = -1$. As discussed above, dynamics for the other chirality are obtained by reflection about the x axis.

We begin with the fully deterministic system, later adding orientational and translational diffusion. The fully deterministic case ($\gamma_t = \gamma_o = 0$) is accessible to large ($> 100\ \mu$m) swimmers whose potential-free trajectories are almost perfect circles [29]. We mapped out the swimmer behavior with a resolution of $\Delta\alpha = 0.01$, $\Delta\beta = 0.5$ to obtain the "drift-phase diagram" shown at the center of Fig. 1. At each (α, β) value, trajectories were calculated starting from 12 initial conditions distributed uniformly over a fundamental unit cell of the potential. We used an Euler algorithm with 360β and 3600β time steps per rotational period to make sure the discretization does not affect the trajectories in the drift regimes of deterministic dynamics. For each initial condition and time step, we simulated for 100 periods, which was verified to be more than sufficient for convergence to an attractor. We observed collapse onto a unique trajectory attractor independent of initial condition, generally, within a few periods for nearly all (α, β) values (see middle right of Fig. 1). Exceptions were observed for $6 \le \beta \le 7$ and $\alpha \approx 0.6$, and also in the complicated region around $1.0 \le \alpha \le 1.2$, $\beta \approx 4$. However, these effects are washed out by introducing stochastic noise.

The chiral swimmer executes closed orbits—no net drift—at both weak and strong potential amplitude α. Potentials of intermediate strength host a variety of steady drift behaviors over well-defined regions of the $\alpha - \beta$ plane, usually at a speed v_β of one lattice constant per rotation period, $v_\beta = 2v_0/(\sqrt{3}\beta)$. Except for a narrow sliver at large β and small α, the drift velocity has a non-negative x

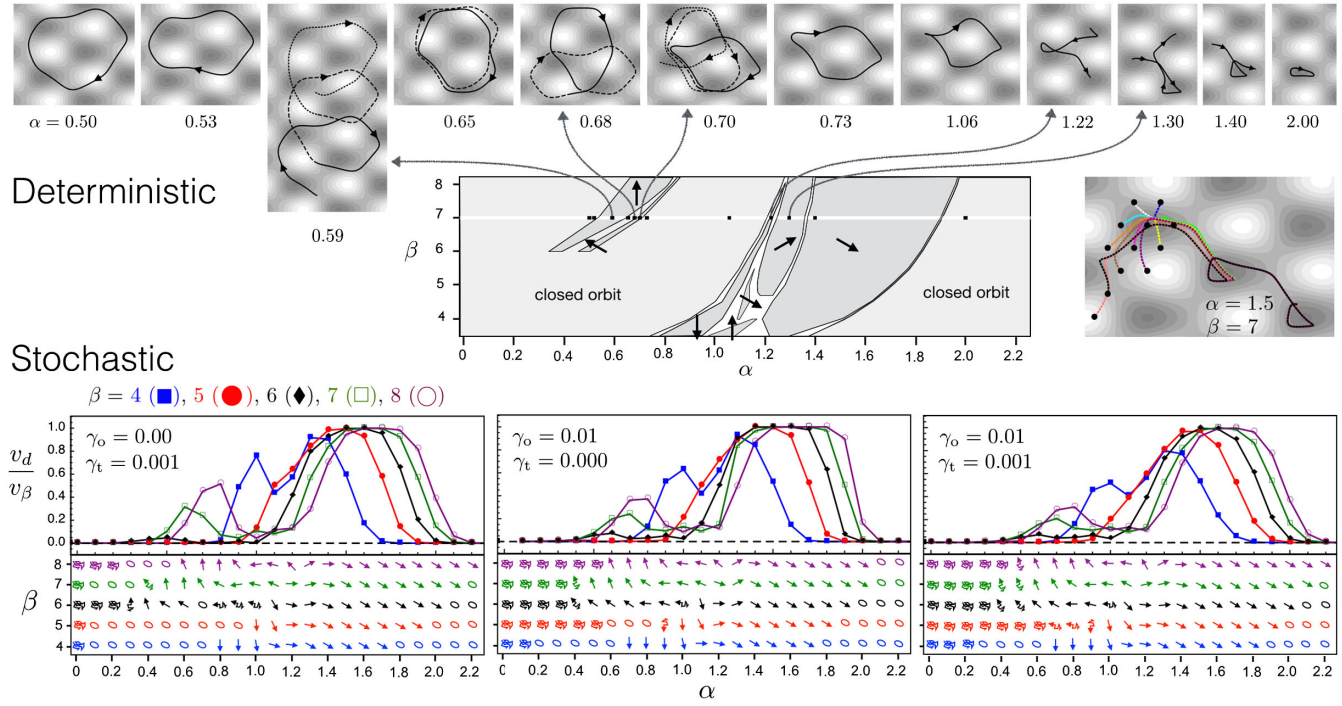

FIG. 1 (color online). Drift-phase behavior for the counterclockwise chiral swimmer without ("deterministic") and with ("stochastic") orientational and translational diffusion. The deterministic drift-phase diagram has regions of closed orbits and also drift regions marked by arrows at $\pm 30°$, $\pm 90°$, or $150°$. Dots on the white band at $\beta = 7.0$ indicate the points for which representative trajectory attractors are shown along the top row. With increasing α, these attractors evolve to encircle different maxima or surmount different saddle points, as described in the main text. The stochastic systems with modest orientational (γ_o) and/or translational (γ_t) diffusion show more variable drift speeds v_d, as shown in the bottom row of panels for $\beta = 4, 5, 6, 7, 8$ as filled square, filled circle, filled diamond, square, circle, also color coded to match the rows of drift-direction symbols below. Each data point is an average over the drift velocities for 12 initial conditions uniformly distributed in the fundamental unit cell of the periodic potential. Drift directions are shown by a separate plot with an array of symbols as a function of α and β. Closed ellipses indicate localization. Straight arrows indicate uniform drift with less than one degree variance in direction. Squiggly arrows indicate drift with significant wandering [directional variance about $\mathcal{O}(10°)$]. The symbol indicates diffusive behavior. The plot at center right shows a typical rapid coalescence of trajectories starting from different locations, here within two orbital periods at $(\alpha, \beta) = (1.5, 7.0)$.

component. Within the white, unshaded portion of the drift-phase diagram, the trajectories are more complex and repeat only after many orbital periods. This finely tuned high-period behavior is washed out by weak stochastic noise, as discussed later.

The "tongue" around $\beta \approx 7$ and $\alpha \approx 0.6$ defines an interesting reentrant behavior as a function of α for fixed β. This reentrance is associated with transitions in the number of maxima enclosed by the rotor trajectory, as illustrated by the trajectory attractors on the top row of Fig. 1. At the smallest values of α (i.e., weak potential), the orbit encloses three maxima and is only weakly perturbed from circularity. A transition from three to two enclosed maxima, which occurs around $\alpha = 0.51$, sets the stage for the emergence of drift behavior at slightly larger values of α. In this regime, multiple distinct pairs or trios of maxima compete for the prize of enclosure, and drift occurs when the system "side steps" through lattice vectors of the potential as it transitions between topologically distinct choices of enclosed maxima, as shown in Fig. 1 for $\alpha = 0.59$ and 0.70. A narrow fjord with high-period closed orbits separates these drift regions, with structure that also indicates competition between maxima. The local phase space expansion rate is proportional to $-\nabla^2 V$, so a slight shift in the attractor near a potential maximum entails relatively large changes elsewhere, thus helping explain the sensitive dependence of the trajectory on the particular maxima enclosed. At $\alpha = 0.70$, the drift involves transitions between a pair of maxima and just a single maximum; this presages the end of the reentrant "tongue" and the emergence of a broad, stable region of closed orbits where only a single maximum is enclosed, as exemplified by $\alpha = 0.73$ and 1.06. Drift then reasserts itself around $\alpha \approx 1.2$, where the potential first becomes strong enough that the rotor cannot surmount a saddle point; the resulting drift orbits at higher α enclose *zero* maxima and are characterized by which saddle points are surmounted. The reentrant tongues terminate at smaller values of β where the potential period is too large for the attractor to ever surround three maxima.

Rather than simply obliterating the finer features of the deterministic drift-phase diagram, modest amounts of stochastic noise in the form of orientational or translational diffusion actually expand the domain of drift behavior and greatly accentuate the degree of leftward drift, as shown by array of drift directions in the bottom row of panels in Fig. 1 for $(\gamma_o, \gamma_t) = (0, 0.001)$, (0.01,0), and (0.01,0.001). Each data point averages over 12 initial condition for 2000 periods of deterministic rotation. Since the drift speed (and sometimes direction) in the stochastic case changes continuously with α and β, the results are plotted differently from the deterministic case: with a dense grid of arrows showing drift directions, plus the drift speed in a second panel. The thin sliver of leftward drift in the deterministic diagram opens up into a broad region of generally leftward motion. The large region of $-30°$ drift in the deterministic diagram is robust against modest stochastic orientational or translational noise, preserving its direction with only a small reduction in speed as occasional saddle point transitions are missed due to noise. This down-right drift domain actually expands to cover larger values of α where the deterministic orbits are closed: in this extended domain, occasional stochastic kicks facilitate saddle point transitions in a process akin to stochastic resonance. A well-defined plateau with a steady near-ideal ($v_d \approx v_\beta$) drift speed to the lower right exists across a wide range of α and β, indicating that broad populations of swimmers can be directed on nearly uniform chirality-dependent trajectories. For the weakest potentials, the closed orbits of the deterministic case open up into diffusive trajectories marked by the symbol 🔀. Perfect localization cannot persist indefinitely in the presence of even the slightest amount of noise. The real meaning of the closed orbit symbols in Fig. 1 is observed localization over at least 2000 periods.

At a fixed finesse β, it is possible to steer swimmers of a given chirality to an arbitrary location using only variations in the strength of the potential. The requirement is three drift vectors such that all of their mutual nearest-neighbor angles are less than 180°. Three rather than two such basis vectors are needed, since only positive coefficients are allowed in their superposition. Such triples can be identified for some values of β on the drift diagrams of Fig. 1. For example, for a swimmer of characteristics $(\gamma_o, \gamma_t) = (0.01, 0)$ operating in a $\beta = 7.0$ potential, any desired displacement can be obtained by dwelling for controlled periods of time at $\alpha = 0.9, 1.3$, and 1.7. This effect is obtainable across a range of values of diffusivities γ_o and γ_t, most commonly, at the larger values of β. Note also that iterations of the procedure could be used to compensate for random motions.

Keeping in mind that the amplitude and scale parameters α and β are made dimensionless through incorporation of v_0 and ω, these drift-phase diagrams also provide a means to distinguish swimmers based on their linear or angular speeds. Numerous schemes can be designed to affect this outcome. For example, filtering out of everything but horizontal right movers will select for just those swimmers whose specific values of v_0 and ω place them in the restricted region of pure rightward drift for a given inverse lattice constant K and potential amplitude C. The video in Supplemental Material [30] provides one example of differential drift for motors with different linear or angular velocities in the same potential. More generally, the potential strength can be slowly varied in space to create boundaryless fluidic circuits where different drift velocities are designed to occur in different regions of the plane.

With increasing strength of the stochastic terms, the drift-phase diagram smooths out and the downright motion begins to dominate, as shown in Supplemental Material [30]. Since this dominant drift direction retains a large vertical component, robust chiral separation is still possible if one accepts (or exploits) variations in drift speed, but more complex steering or fluidic circuits are less practical in this limit. Even at high stochasticity, there remains an interesting region of incipient drift on the low-α side of the main drift peak, marked by the symbol 🔀, where the motion looks something like a biased Brownian diffuser.

With a range of propulsive mechanisms and motor geometries now in hand for autonomous movers, their separation and guidance at the micro- or nanoscales becomes a natural next goal. A soft periodic potential designed to express prescribed spatial symmetries provides an intriguing framework in which to control the long-time, long-distance behavior of rotary swimmers, particularly since both optical and acoustic fields are available to provide the requisite spatially and temporally tunable potentials. Chiral swimmers separated by handedness, speed and orbital frequency should then become available for further tasks, whether of a practical or fundamental nature. Interactions between the swimmers provide further prospects for interesting behavior. Weak short-range interactions within dilute swimmer populations may act something like a stochastic term; at higher motor concentrations, a reasonably long-ranged attractive interaction could possibly lead to locking of drift speeds for nearby motors. Stronger interactions could conceivably generate complex collective drift behaviors.

This work was supported by the National Science Foundation under Grants No. DMR-0820404 and DMR-1420620 through the Penn State Center for Nanoscale Science.

*nourhani@psu.edu

[1] *Chiral Separations Methods and Protocols*, 2nd ed. edited by G. K. E. Scriba (Humana Press, New York, 2013).
[2] P. G. de Gennes, Europhys. Lett. **46**, 827 (1999).
[3] M. Kostur, M. Schindler, P. Talkner, and P. Hänggi, Phys. Rev. Lett. **96**, 014502 (2006).

[4] D. Speer, R. Eichhorn, and P. Reimann, Phys. Rev. Lett. **105**, 090602 (2010).
[5] L. Bogunovic, M. Fliedner, R. Eichhorn, S. Wegener, J. Regtmeier, D. Anselmetti, and P. Reimann, Phys. Rev. Lett. **109**, 100603 (2012).
[6] R. Eichhorn, Phys. Rev. Lett. **105**, 034502 (2010).
[7] S. Meinhardt, J. Smiatek, R. Eichhorn, and F. Schmid, Phys. Rev. Lett. **108**, 214504 (2012).
[8] A. Nourhani, Y.-M. Byun, P. E. Lammert, A. Borhan, and V. H. Crespi, Phys. Rev. E **88**, 062317 (2013).
[9] S. Kudo, N. Imai, M. Nishitoba, S. Sugiyama, and Y. Magariyama, FEMS Microbiol. Lett. **242**, 221 (2005).
[10] I. H. Riedel, K. Kruse, and J. Howard, Science **309**, 300 (2005).
[11] G. Li, L.-K. Tam, and J. Tang, Proc. Natl. Acad. Sci. U.S.A. **105**, 18355 (2008).
[12] P. D. Frymier, R. M. Ford, H. C. Berg, and P. T. Cummings, Proc. Natl. Acad. Sci. U.S.A. **92**, 6195 (1995).
[13] R. Laocharoensuk, J. Burdick, and J. Wang, ACS Nano **2**, 1069 (2008).
[14] P. Dhar, T. Fischer, Y. Wang, T. Mallouk, W. Paxton, and A. Sen, Nano Lett. **6**, 66 (2006).
[15] E. Lauga, W. R. Diluzio, G. M. Whitesides, and H. A. Stone, Biophys. J. **90**, 400 (2006).
[16] S. Fournier-Bidoz, A. C. Arsenault, I. Manners, and G. A. Ozin, Chem. Commun. (Cambridge), 441 (2005).
[17] L. Qin, M. J. Banholzer, X. Xu, L. Huang, and C. A. Mirkin, J. Am. Chem. Soc. **129**, 14870 (2007).
[18] Y. Wang, S. to Fei, Y.-M. Byun, P. E. Lammert, V. H. Crespi, A. Sen, and T. E. Mallouk, J. Am. Chem. Soc. **131**, 9926 (2009).
[19] J. G. Gibbs, S. Kothari, D. Saintillan, and Y. P. Zhao, Nano Lett. **11**, 2543 (2011).
[20] A. Nourhani, P. E. Lammert, A. Borhan, and V. H. Crespi, Phys. Rev. E **89**, 062304 (2014).
[21] S. van Teeffelen and H. Löwen, Phys. Rev. E **78**, 020101 (2008).
[22] B. M. Friedrich and F. Jülicher, New J. Phys. **10**, 123025 (2008).
[23] S. Ebbens, R. A. L. Jones, A. J. Ryan, R. Golestanian, and J. R. Howse, Phys. Rev. E **82**, 015304 (2010).
[24] C. Weber, P. K. Radtke, L. Schimansky-Geier, and P. Hänggi, Phys. Rev. E **84**, 011132 (2011).
[25] D. Takagi, A. B. Braunschweig, J. Zhang, and M. J. Shelley, Phys. Rev. Lett. **110**, 038301 (2013).
[26] A. Nourhani, P. E. Lammert, A. Borhan, and V. H. Crespi, Phys. Rev. E **87**, 050301(R) (2013).
[27] C. Reichhardt and C. J. Olson Reichhardt, Phys. Rev. E **88**, 042306 (2013).
[28] M. Mijalkov and G. Volpe, Soft Matter **9**, 6376 (2013).
[29] D. Ahmed, M. Lu, A. Nourhani, P. E. Lammert, Z. Stratton, H. S. Muddanna, V. H. Crespi, and T. J. Huang, Sci. Rep. **5**, 9744 (2015).
[30] See Supplemental Material at http://link.aps.org/supplemental/10.1103/PhysRevLett.115.118101 for depictions of drift behavior at additional values of stochasticity, and samples of detailed trajectory behavior.